AIAA JOURNAL
Vol. 47, No. 2, February 2009

Model for Deformation of Drops and Liquid Jets in Gaseous Crossflows

A. Mashayek*
University of California San Diego, La Jolla, California 92093-0411
and
N. Ashgriz†
University of Toronto, Toronto, Ontario M2M 2G5, Canada

DOI: 10.2514/1.36148

An analytical–numerical model is developed to calculate the deformation and spreading of axisymmetric and two-dimensional liquid drops in a gas stream for small Ohnesorge numbers and large Reynolds numbers. The model is based on an approximate series solution of the Navier–Stokes equations written for the interior flow of the drop and assuming a quasi-static gas flow. The pressure distribution on the drop surface is provided using a perturbation analysis about a trivial zeroth-order solution. The axisymmetric formulation is used for calculating the deformation of the spherical droplets, and the two-dimensional formulation is used to develop a model for predicting the spreading of the cross section of liquid jets in crossflows. The penetration of the liquid jet in the gas flow is calculated, and the results are compared with experimental and empirical results.

Nomenclature

A	=	series coefficient
a	=	series coefficient, spreading radius
k	=	viscosity ratio
M	=	momentum ratio
Oh	=	Ohnesorge number
p	=	pressure
q	=	density ratio
r	=	radial coordinate, radius
Re	=	Reynolds number
Re_l	=	Reynolds number defined based on the liquid properties
t	=	time
U, u	=	velocity
We	=	Weber number
Z	=	flow direction
θ	=	meridional angle
μ	=	viscosity
ρ	=	density
σ	=	surface tension

Subscripts

g	=	gas
i, j	=	series coefficient subscript
l	=	liquid
r	=	radial direction
z	=	axial direction
∞	=	free stream

Received 11 December 2007; revision received 29 August 2008; accepted for publication 22 September 2008.

*Graduate Research Assistant, Department of Mechanical and Aerospace Engineering.

†Professor, Department of Mechanical and Industrial Engineering, 5 King's College Road, Phone: (416) 946-3408; Fax: (416) 978-3453; Ashgriz@mie.utoronto.ca.

I. Introduction

OVER the past years, an extensive amount of research has been dedicated to studying the motion of a liquid drop in a gaseous medium. Several research papers and books have been published on the mechanism of motion and deformation of drops and different breakup regimes associated with high deforming particles. These types of studies contribute to various scientific and industrial applications such as fuel injection in aerial and automotive engines and the coating industry, among others. Drop deformation and breakup in high Reynolds number flows in particular has applications in fuel injections and has been studied extensively in single drop or multidrop systems such as sprays. A review on some experimental investigations can be found in Wierzba [1]. Among the experimental studies dedicated to drop deformation at high Reynolds numbers are Ranger and Nicholls [2], Gelfand et al. [3], and Hirahara and Kawahashi [4]. Some theoretical works on drop motion and deformation at high Reynolds numbers include Harper and Moore [5], Gonor and Zolotova [6], and Fornberg [7], and among some recent numerical studies on this subject are Helenbrook and Edwards [8], Constantinescu and Squires [9], Quan and Schmidt [10], and Wadhwa et al. [11].

In addition to spherical drops, injection of a liquid jet into a gaseous crossflow (JICF) has applications in fuel injection systems such as gas turbines, afterburners, augmenters, and ramjet–scramjet combustors. This type of fuel injection improves the fuel atomization and vaporization processes and is commonly used in lean, premixed, prevaporized combustion systems. The deformation of the liquid jet and the blockage it imposes on the flow changes the gas flowfield significantly. The breakup regimes involved in this type of atomization can be very complex and depend significantly on the aerodynamic forces that affect the jet deformation and spreading, its deflection, and the rate of mass stripping from it. Mazallon et al. [12] experimentally investigated the primary breakup of laminar round liquid jets in gaseous crossflows. They suggested that there are qualitative similarities between the deformation of nonturbulent round liquid jets in crossflows and the deformation of drops in gas flows. This similarity has been reported in a number of other papers. In this paper, we investigate this similarity to gain a better perception of low deformations and penetration of liquid jets in a crossflow. We start by developing a model to describe the deformation of a two-dimensional (2-D) drop in a gas flow and use this model to calculate the deformation of the cross section of a liquid jet in a crossflow under certain conditions. Several works have used simple models, which allowed the cross section of the jet to deform into simple

geometries such as an ellipse, to calculate the penetration of the jet. Among these studies are Nguyen and Karagozian [13] and Mashayek et al. [14]. In this work, we extend those studies by providing a realistic estimate of the deformation of the liquid jet based on the solution of the Navier–Stokes equations. The more accurate the deformation of the liquid jet is predicted, the better the penetration of the jet is calculated. Mashayek et al. [14] presented a comprehensive review on the works done on predicting the penetration of a liquid jet in a subsonic crossflow.

In Sec. II of this paper, we leverage a theoretical model initially proposed by Gonor and Zolotova [6], and after few additions and modifications, we develop a numerical scheme to calculate the motion and deformation of an axisymmetric liquid drop in a gaseous flow for cases with small Ohnesorge and large Reynolds numbers. The model is modified to solve for the motion of two-dimensional drops in Sec. III, and finally, the model developed in Sec. III is used to model the jet deformation and penetration in Sec. IV.

II. Deformation of an Axisymmetric Drop

In this section we consider the motion of an axisymmetric liquid drop located in an incident uniform gas flow with velocity U_g as shown in Fig. 1.

Assuming that the gas speed is well below the speed of sound, the gas phase can be considered incompressible, and both the gas flow and the flow inside the drop are governed by the incompressible Navier–Stokes equations. To characterize the flow, we chose four dimensionless parameters, namely the liquid-to-gas density ratio $q = \rho_l/\rho_g$, the liquid-to-gas dynamic viscosity $k = \mu_l/\mu_g$, the Weber number $We = \rho_g U_g^2 r_0/\gamma$, and the Reynolds number $Re = \rho_g U_g r_0/\mu_l$, where μ_l and μ_g are the dynamic viscosities, and ρ_l and ρ_g are the densities of the liquid and gas phases, respectively, r_0 is the initial radius of the drop, and γ is the surface tension of the liquid. Helenbrook and Edwards [8] showed that the rate of change of the drop velocity can be estimated by $18q\nu_g/r_0^2$, and for Ohnesorge numbers much less than one the oscillation decay rate of a drop is given by $20\nu_l/r_0^2$, where ν_l and ν_g are the kinematic viscosities of the liquid and gas phase, respectively. Dividing the later by the former we get $10k/9$, which physically means that for high density ratios, the drop deformation rate is much larger than the rate of change of the relative velocity of the gas and the drop. Thus, the drop responds in a quasi-steady manner to the instantaneous relative velocity between the drop and the gas. In other words, for relative velocities of the order of several tens of meters, the characteristic time of the gas flow passing over a drop U_g/r_0 is very small compared with the characteristic time of drop deformation. Therefore, the gaseous flow can be estimated by a quasi-stationary uniform flow over a deforming drop. These flow conditions occur in various real applications, such as in drop deformation in spray systems, where the drop size is small relative to the flow scales and its deformation rate is fast compared with the change in the relative velocity of the incident gas flow. A more detailed analysis of the time scales of quasi-steady deformation of liquid drops is presented in Helenbrook and Edwards [8].

Based on the preceding discussion, the effect of the deformation of the drop on the gas flow is of higher order. Therefore, assuming a uniform quasi-steady gas flow over the sphere is accurate to the leading order. Thus, we focus on the deformation of the drop, and write down the system of equations governing the motion of the drop in cylindrical coordinates in the form of

$$\frac{\partial u_z}{\partial t} + u_z\frac{\partial u_z}{\partial z} + u_r\frac{\partial u_z}{\partial r} = -\frac{1}{q}\frac{\partial p}{\partial z} + \frac{1}{Re}\left(\frac{\partial^2 u_z}{\partial z^2} + \frac{\partial^2 u_z}{\partial r^2} + \frac{1}{r}\frac{\partial u_z}{\partial r}\right) \tag{1}$$

$$\frac{\partial u_r}{\partial t} + u_r\frac{\partial u_r}{\partial z} + u_r\frac{\partial u_r}{\partial r} = -\frac{1}{q}\frac{\partial p}{\partial r} + \frac{1}{Re}\left(\frac{\partial^2 u_r}{\partial z^2} + \frac{\partial^2 u_r}{\partial r^2} + \frac{1}{r}\frac{\partial u_r}{\partial r} - \frac{u_r}{r^2}\right) \tag{2}$$

$$\frac{\partial u_z}{\partial z} + \frac{\partial u_r}{\partial r} + \frac{u_r}{r} = 0 \tag{3}$$

Equations (1–3) are nondimensionalized using $t' = tu_g/r_0$, $u' = u/U_g$, $r' = r/r_0$, and $p' = p/\rho_g U_g^2$, where r_0 is the initial drop radius.

A. Boundary Conditions

To construct any analytical or numerical solution, one must satisfy the necessary boundary conditions on the gas–liquid interface, which include the jump in the normal stress across the interface, the continuity of the shear stress across the interface in the absence of surfactants, and the continuity of the velocities on the interface. To derive the mathematical expressions for the boundary conditions in studies of two-fluid flows, it is often convenient to express the gas–liquid interface in the form of a material surface $F(z, r, \varphi, t) = 0$ [15]. This function describes the location of a material surface in Eulerian form and satisfies an evolution equation that emerges by requiring that the motion of the point particles on the material surface is consistent with the deformation of the material surface as described in the Eulerian form [15]. The evolution equation for our axisymmetric drop is

$$\frac{DF}{Dt} = \frac{\partial F}{\partial t} + \mathbf{u}\cdot\nabla F = \frac{\partial F}{\partial t} + u_r\frac{\partial F}{\partial r} + u_z\frac{\partial F}{\partial z} = 0 \tag{4}$$

The boundary conditions require that the traction undergo a discontinuity across an interface. Naming the traction tensors in the liquid and gas phases by $\mathbf{f}_l$, $\mathbf{f}_g$, respectively, we can write

$$\Delta\mathbf{f} = \gamma\mathbf{n}\nabla\cdot\mathbf{n} - (\mathbf{I} - \mathbf{nn})\cdot\nabla\gamma \tag{5}$$

where $\nabla\mathbf{f} = \mathbf{f}_g - \mathbf{f}_l$ and $\mathbf{n}$ are the unit vector normal to the interface pointing into the gas phase. The first term on the right side of Eq. (5) expresses the discontinuity of traction in the normal direction, and the second term is the discontinuity in the tangential direction (noting that $(\mathbf{I} - \mathbf{nn})$ extracts the tangential component of a vector). Focusing on the normal component, projecting Eq. (5) on the normal direction, noting that $\nabla\cdot\mathbf{n} = 2\kappa_m$, and noting that the normal component of the traction in each fluid can be written as $\mathbf{f}^N = [-p + 2\mu\mathbf{n}\cdot(\nabla\mathbf{n})\cdot\mathbf{n}]\mathbf{n}$, we have

$$\Delta\mathbf{f}\cdot\mathbf{n} = -p_g + p_l + 2\mathbf{n}\cdot(\mu_g\nabla\mathbf{u}_g - \mu_l\nabla\mathbf{u}_l)\cdot\mathbf{n} = 2\gamma\kappa_m \tag{6}$$

where κ_m is the mean curvature of the interface. Expressing the normal vector in terms of the material surface function by $\mathbf{n} = \nabla F/|\nabla F|$, noting that $\mu_g \ll \mu_l$, and nondimensionalizing the parameters in Eq. (6) similar to Eq. (1), we get

$$\begin{aligned}\Delta p = p_g - p_l &= -(2q/Re)\mathbf{n}\cdot(\mu_l\nabla\mathbf{u}_l)\cdot\mathbf{n} - 2\kappa_m/We \\ &= \frac{-2q}{Re(F_r^2 + F_z^2)}\left[\frac{\partial u_r}{\partial r}F_r^2 + \frac{\partial u_z}{\partial z}F_z^2 + \left(\frac{\partial u_r}{\partial z} + \frac{\partial u_z}{\partial r}\right)F_rF_z\right] \\ &\quad - 2\kappa_m/We\end{aligned} \tag{7}$$

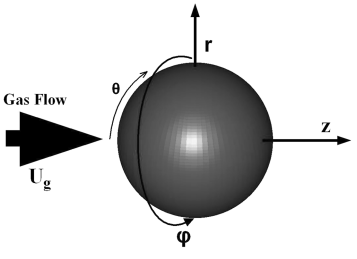

Fig. 1 Schematic of an axisymmetric drop in uniform gas flow.

The mean curvature κ_m can be calculated as $0.5(1/R_1 + 1/R_2)$, where $1/R_1$ and $1/R_2$ are the principle curvatures of the interface. The mean curvature can be expressed in terms of the material surface $F(z, r, t) = 0$ in the form of [15]:

$$\kappa_m = \frac{1}{2}\nabla \cdot \mathbf{n} = \frac{1}{2}\nabla \cdot \left(\frac{\nabla F}{|\nabla F|}\right) = \frac{1}{2}\frac{\partial}{\partial x_i}\left[\frac{\partial F}{\partial x_i}\Big/\left(\frac{\partial F}{\partial x_j}\frac{\partial F}{\partial x_j}\right)^{1/2}\right] \quad (8)$$

Focusing on the second term of in Eq. (5), it is seen that in the absence of surfactants, the surface tension on the interface is constant and the traction does not suffer a discontinuity in the tangential direction. Thus, the shear stress is continuous across the interface, and we can write

$$\mathbf{f}_g^T = \mathbf{f}_l^T = 2\mu_l \mathbf{n} \times (\mathbf{n} \cdot \mathbf{E}) \times \mathbf{n} \quad (9)$$

where E is the rate of deformation tensor. Projecting Eq. (9) onto the tangential direction, using $E_{ij} = \frac{1}{2}(\frac{\partial u_j}{\partial x_i} + \frac{\partial u_i}{\partial x_j})$ for an incompressible flow, and using $\mathbf{n} = \nabla F/|\nabla F|$ again, we get

$$\tau = \frac{q}{Re(F_r^2 + F_z^2)}\left[\left(\frac{\partial u_z}{\partial r} + \frac{\partial u_r}{\partial z}\right)(F_z^2 - F_r^2) + 2\left(\frac{\partial u_z}{\partial z} - \frac{\partial u_r}{\partial r}\right)F_r F_z\right] - 2\kappa_m/We \quad (10)$$

We must ensure that the condition of the continuity of the velocity across the interface is satisfied at all times. We will return to this discussion once the flow surrounding the drop is described in more details.

1. Perturbation Analysis

Following the original perturbation method used by Gonor and Zolotova [6], we construct a solution by perturbing the pressure on the drop surface. To do this, we shall look for a simple solution of the system of Eqs. (1–3) to form the zeroth-order approximation. Figure 2 shows the pressure distribution on a solid sphere subjected to gas flow at various Reynolds numbers. The meridional angle θ is shown in Fig. 1. Curve a in the figure corresponds to a potential flow past a sphere. In the absence of viscosity, the sum of the pressure and velocity heads remains constant as we move along the contour of the sphere in the meridional plane according to the Bernoulli equation. This means that the pressure head decreases as θ increases from zero while the velocity head increases up to the point of $\theta = \pi/2$. From this point on, the decrease in the velocity head contributes to the increase in the pressure head until it reaches its initial value again at $\theta = \pi$. In the presence of viscosity, however, the pressure head cannot recover all of its initial value due to viscous losses along the way, and, thus, the flow separates at some point on the sphere wall and a wake forms behind the sphere. This phenomenon changes the pressure distribution on the sphere as shown in Fig. 2 for various Reynolds numbers. As the figure shows, the pressure distribution on the sphere remains not much changed for a wide range of Reynolds numbers in the range $\sim$1000 and $\sim 10^5$, which covers a broad variety of applications such as liquid deformation in spray systems. It should be noted that the pressure curves almost coincide for $\theta \in (0, \pi/2)$ and have a nearly linear profile. Thus, a reasonable approximation for the zeroth order part of the solution is line (g) in the figure. However, other linear approximations such as a linear fit to the whole curves (rather than the first half) can be chosen as a zeroth-order approximation. A third alternative can be the curve of the potential flow, curve a.

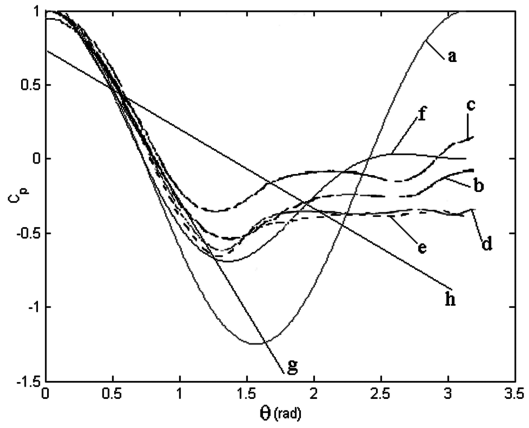

Fig. 2 Pressure coefficient C_p over a solid sphere, with a) potential flow, b) $Re = 500$ (Fornberg [7]), c) $Re = 1000$ (Fornberg [7]), d) $Re = 10^4$ (Constantinescu and Squires [9]), e) $Re = 10^5$ (Constantinescu and Squires [9]), f) smoothed potential curve, g) $\theta = 60$ linear approximation, and h) a general linear curve fit.

In this section, we follow Gonor and Zolotova [6] and choose a flow with a linear pressure profile as the zeroth-order approximation for the solution of the drop motion. Thus, the zeroth-order pressure gradient on the sphere is expressed in the form of

$$\frac{\mathrm{d}p_g^0}{\mathrm{d}z} = C(t) \quad (11)$$

where C is the slope of line (g) in Fig. 2 and the superscript "0" denotes the zeroth-order approximation. It will be shown in Eq. (25) that $\frac{\partial p_g^0}{\partial z} = \frac{\partial p_l^0}{\partial z}$, meaning that the pressure distribution on the liquid side of the interface is also linear in the zeroth order [based on the assumption made in Eq. (11)] and has the same slope as the distribution on the gas phase side of the interface. Thus, p_l^0 is also only a function of coordinate z and using Eq. (2), we find $u_r^0 = 0$. In the zeroth order approximation, Eq. (4) reduces to

$$\frac{DF}{Dt} = \frac{\partial F_0}{\partial t} + u_z^0 \frac{\partial F_0}{\partial r} = 0 \quad (12)$$

with the initial condition $F(z, r, 0) = r^2 + z^2 - 1 = 0$. As shown by Gonor and Zolotova [6], the solution of Eq. (12) is

$$F_0(z, r, 0) = r^2 + (z - z_0)^2 - 1 = 0 \quad (13)$$

which shows that the geometry that corresponds to the linear choice of the zeroth-order pressure made in Eq. (11) is a sphere (nondeforming drop) moving with the velocity of $u_z^0 = \mathrm{d}z_0/\mathrm{d}t$.

To calculate the constant C in Eq. (11), we use curve a and express the pressure distribution of a potential flow over a sphere in the form of

$$P = P_\infty + \frac{1}{2}\rho_\infty (V_\infty - u_{\mathrm{drop}})^2 (1 - n\sin^2(\theta)) \quad (14)$$

Nondimensionalizing the parameters similar to Eqs. (1–3), transferring to cylindrical coordinates by setting $z = -\cos(\theta)$, using the value of $n = 9/4$ for an axisymmetric drop, and calculating the slope of the pressure curve a at $z = -1/2$ ($\theta = 60$ deg in Fig. 2), we get

$$\frac{\mathrm{d}p_g^0}{\mathrm{d}z} = -\frac{n}{2} nz(1 - u_z^0)^2 = -\frac{9}{8}\left(1 - u_z^0\right)^2 \quad (15)$$

Noting again that $\frac{\partial p_g^0}{\partial z} = \frac{\partial p_l^0}{\partial z}$, replacing Eq. (11) into Eqs. (1) and (2), and noting that u_z^0 is only a function of time and $u_r^0 = 0$ in the zeroth approximation, we have

$$\frac{\mathrm{d}u_z^0}{\mathrm{d}t} = -\frac{1}{q}\frac{\mathrm{d}p_g^0}{\mathrm{d}z} \quad (16)$$

Combining Eqs. (14) and (16) and solving for u_z^0 we get

$$u_z^0(t) = \frac{lt}{1 + lt} \quad (17)$$

where $l = 9/(8q)$.

Following the discussion presented earlier, one can assume that the pressure distribution on the drop changes in a quasi-static manner compared with the deformation of the drop. As shown by Helenbrook and Edwards [8], for cases with $Oh \sim 1$, the drops are under-damped and the gas flow can be assumed quasi-static provided, that the viscosity ratio k is large enough. Defining $\varepsilon = 1/k$, we can perturb the pressure distribution about the linear profile presented by the straight line in Fig. 2 in the form of

$$p_g = p_g^0 + \varepsilon p_g^1 + O(\varepsilon^2) \tag{18}$$

Expanding the parameters of the interior flow (flow inside the drop) in the same manner we have

$$\begin{aligned} p_l &= p_l^0 + \varepsilon p_l^1 + O(\varepsilon^2) \\ u_z &= u_z^0 + \varepsilon u_z^1 + O(\varepsilon^2) \\ u_r &= \varepsilon u_r^1 + O(\varepsilon^2) \end{aligned} \tag{19}$$

where $u_r^0 = 0$. The expansions in Eq. (19) express that the motion of a liquid drop can be expressed as the sum of the linear motion of a noninertial frame of reference attached to the nondeforming drop in the zeroth-order solution (u_z^0), and the motion of the liquid relative to this noninertial frame [terms of order ε in Eq. (19)]. This will yield an error of $O(\varepsilon^2)$ in the coordinate systems. Thus, to calculate the motion of the drop, one can first solve for the linear velocity of the noninertial frame, which counts for the translation of the drop in the z direction. This can be easily done by integrating Eq. (17) to find the displacement of the drop in the zeroth-order approximation. However, the assumed zeroth-order pressure distribution does not count for the complicated physics associated with the flow separation and the vortex structures in the wake of the spherical drop and, thus, cannot provide an accurate estimate of the drop translation. Numerous experimental and theoretical studies have been devoted to calculate the drag coefficient of a liquid drop in a high-speed gas flow. Reliable formulae and correlations have been derived to calculate the translation of a drop subjected to various flow conditions. The focus of the present paper is on the deformation of the drop and calculation of the first-order terms of the expansions of Eq. (19). The zeroth order term can be calculated using well-established works and correlations [2,5].

Rewriting the z-direction Navier–Stokes equation in the noninertial frame, the velocities of the fluid are expressed by εu_z^1 and εu_r^1, and we have

$$\begin{aligned} \varepsilon \frac{\partial u_z}{\partial t} + \varepsilon^2 u_z \frac{\partial u_z}{\partial z} + \varepsilon^2 u_r \frac{\partial u_z}{\partial r} &= -\frac{1}{q}\frac{\partial p}{\partial z} \\ + \frac{1}{Re}\left(\varepsilon \frac{\partial^2 u_z}{\partial z^2} + \varepsilon \frac{\partial^2 u_z}{\partial r^2} + \varepsilon \frac{1}{r}\frac{\partial u_z}{\partial r}\right) &+ F^{\text{inertial}} \end{aligned} \tag{20}$$

where F^{inertial} is the fictitious inertial force, because the equation is not written in an inertial frame. Generally, F^{inertial} is a function of the linear and rotational velocities and accelerations of the moving frame. For the present case, F^{inertial} reduces to $-\mathrm{d}u_z^0/\mathrm{d}t$. Neglecting higher order terms in Eq. (20), noting that $\partial p/\partial z = \partial p^0/\partial z + \varepsilon \partial p^1/\partial z$, and using Eq. (16), we get

$$\frac{\partial u_z^p}{\partial t} = -\frac{1}{q}\frac{\partial p^p}{\partial z} + \frac{1}{Re}\left(\frac{\partial^2 u_z^p}{\partial z^2} + \frac{\partial^2 u_z^p}{\partial r^2} + \frac{1}{r}\frac{\partial u_z^p}{\partial r}\right) \tag{21}$$

where $u_z^p = \varepsilon u_z^1$, $u_r^p = \varepsilon u_r^1$, and $p^p = \varepsilon p^1$. Following the same procedure for Eqs. (2) and (3) we get

$$\frac{\partial u_r^p}{\partial t} = -\frac{1}{q}\frac{\partial p^p}{\partial r} + \frac{1}{Re}\left(\frac{\partial^2 u_r^p}{\partial z^2} + \frac{\partial^2 u_r^p}{\partial r^2} - \frac{u_z^p}{r^2}\right) \tag{22}$$

and

$$\frac{\partial u_z^p}{\partial z} + \frac{\partial u_r^p}{\partial r} + \frac{u_r}{r} = 0 \tag{23}$$

The system of Eqs. (21–23) expresses the motion of the particle relative to its local coordinate system and can be solved provided that the proper boundary conditions are satisfied. Because the flow is axisymmetric, we must supply two scalar boundary conditions on each boundary. We can supply two components of the velocity or the two components of traction on the interface or a mixture of both. Focusing on the condition of pressure jump across the interface and expanding the pressure distribution on both sides of the interface with respect to ε, we can write

$$\begin{aligned} \frac{\partial p_g^0}{\partial z} + \varepsilon \frac{\partial p_g^1}{\partial z} &= \frac{\partial p_l^0}{\partial z} + \varepsilon \frac{\partial p_l^1}{\partial z} \\ + \frac{\partial}{\partial z}(-(2q/Re)\mathbf{n} \cdot (\mu_l \nabla \mathbf{u}^l) \cdot \mathbf{n} &- 2\kappa_m/We) \end{aligned} \tag{24}$$

Noting that in the zeroth-order approximation the terms in the parenthesis in the last term of Eq. (24) reduce to a constant, we have

$$\frac{\partial p_g^0}{\partial z} = \frac{\partial p_l^0}{\partial z} \tag{25}$$

which means that the interior zeroth-order pressure also has a linear profile with the same slope and can be expressed as

$$p_l^0 = p_g^0 + c \tag{26}$$

Thus, Eq. (24) reduces to

$$\frac{\partial p_g^p}{\partial z} = \frac{\partial p_l^p}{\partial z} + \frac{\partial}{\partial z}(-(2q/Re)\mathbf{n} \cdot (\mu_l \nabla \mathbf{u}^l) \cdot \mathbf{n} - 2\kappa_m/We) \tag{27}$$

where $p_g^p = \varepsilon p_g^1$, $p_l^p = \varepsilon p_l^1$, and the last term can be calculated using Eq. (8). Equations (24) and (26) are derived for the pressure jump across a spherical drop. However, as the drop deforms, it causes a perturbation in the boundaries of the gas flow of $O(\varepsilon)$. This domain perturbation leads to a perturbation in the outer flow pressure term in Eq. (27) p_g^p of the order of ε. However, because $p_g^p = \varepsilon p_g^1$ is of the order of ε itself, the perturbation of the gas flow boundary leads to a perturbation of $O(\varepsilon^2)$ in the interior flow, which is negligible. This indeed is the consequence of the fact that the gas flow is quasi-stationary. It should be noted that the same argument can be made to show that the component of the velocity normal to the interface can be assumed continuous across the interface. This assumption leads to a perturbation of the boundary of the gas flow by $O(\varepsilon)$ (because the normal velocity in the zeroth order is zero) and has a higher-order influence on the pressure distribution and deformation according to the preceding argument.

As the second boundary condition, the tangential velocity should be continuous across the interface. In reality, a boundary layer develops on the moving surface of the drop, which ensures that the no-slip boundary condition is satisfied on the interface. In the typical range of spray applications, the boundary layer is laminar and the flow over the sphere is thus considered to be subcritical. The thickness of the boundary layer is $O(r_0 Re^{-1/2})$, according to Harper and Moore [5]. Solving the boundary layer equations enables us to calculate the shear stress on the surface of the drop. Noting that the shear stress is continuous across the interface according to Eq. (9) and expanding the shear stress with respect to ε, we have

$$\tau = \tau_0 + \varepsilon \tau_1 = \tau_0 + \tau^p \tag{28}$$

where τ_0 is the zeroth-order term and can be calculated from the solution of the boundary layer over a spherical drop. Harper and Moore developed proper expressions for the shear stress on an almost nondeforming drop at high Reynolds numbers and showed that this stress is proportional to $Re^{-1/2}$. Replacing Eq. (28) in Eq. (10) we have

$$\begin{aligned} \tau^p = -\tau_0 - \frac{q}{Re(F_r^2 + F_z^2)}\Bigg[\left(\frac{\partial u_z}{\partial r} + \frac{\partial u_r}{\partial z}\right)(F_z^2 - F_r^2) \\ + 2\left(\frac{\partial u_z}{\partial z} - \frac{\partial u_r}{\partial r}\right)F_r F_z\Bigg] - 2\kappa_m/We \end{aligned} \tag{29}$$

which can be used to calculate the first order stress on the interface caused by the drop deformation.

2. Solving for the Interface Deformation

Equations (19–21) can be applied to the drop interface $F(z, r, t) = 0$ to calculate its motion. The system of equations can be integrated numerically or solved analytically as done in Gonor and Zolotova [6]. Either way, the terms $\partial p^p/\partial z$ and $\partial p^p/\partial r$ should be provided as a feed to the problem because they are the driving forces that cause the drop to deform from its original spherical shape. Using Eqs. (7), (18), and (26), we can write

$$p_l^p = p_g - p_l^0 + \frac{2q}{Re(F_r^2 + F_z^2)}\left[\frac{\partial u_r}{\partial r}F_r^2 + \frac{\partial u_z}{\partial z}F_z^2 + \left(\frac{\partial u_r}{\partial z} + \frac{\partial u_z}{\partial r}\right)F_r F_z\right] - 2\kappa_m/We + c \tag{30}$$

where κ_m can be calculated from Eq. (8). It should be noted again that p_l^p, p_g, and p_l^0 correspond to the perturbation pressure on the liquid side of the interface, real pressure distribution on the drop, and the zeroth-order approximation of the pressure on the liquid side of the interface. The third term on the right side of Eq. (30) can be calculated at each time step based on the shape of the interface F. Equation (30) suggests that if a proper pressure profile is suggested for p_g, the pressure gradients in Eqs. (21) and (22) can be calculated using Eq. (30) at each time step.

Thanks to numerous experimental and numerical studies done on the problem of a high Reynolds number flow over a sphere or ellipse, for many practical applications a relatively close matching curve can be found for p_g. As shown in Fig. 2, the pressure distribution for Reynolds numbers in the range of few thousand to several tens of thousands are relatively close and the results of Constantinescu and Squires [9] can be used as an example. Curve f in Fig. 2 is produced by multiplying the potential curve a by a smoothing function. The smoothing function used is a polynomial that scales the original curve and flattens the tail of the curve to account for the separation. Because curve f is in good agreement with curves b–e and has a simple analytic form, it can be used as a relatively good choice for p_g. Otherwise, curve fitting seems inevitable. Because the drop deforms into shapes similar to an ellipse in the early stages of its deformation [8,11], as an improvement to the model originally proposed by Gonor and Zolotova, one can use the potential flow over a spheroid along with a smoothing function to calculate p_g. This will build an adaptive pressure distribution calculation for p_g changes as the aspect ratio of the ellipse (the deformed drop) increases from 1. In this paper, however, curve f of Fig. 2 is used as the exterior pressure distribution on the sphere. It should be noted that curves e and d in Fig. 2 correspond to laminar separation over the sphere (subcritical flow), which is consistent with the discussion presented in the previous section regarding the continuity of the tangential stress on the interface.

We now proceed to solve Eqs. (21–23) with the help of Eq. (30) for the interface of the drop $F(z, r, t) = 0$. Following Gonor and Zolotova [6], we expand the z-direction velocity in the form of double series

$$u_z^p = \sum_{i=0}^{\infty}\sum_{j=0}^{\infty} a_{ij}(t) z^i r^{2j} \tag{31}$$

and calculate the corresponding term for u_r^p using Eqs. (23) and (31). Following the mathematical derivations of Gonor and Zolotova closely, we reach the following system of differential equations for the coefficients of Eq. (31):

$$\begin{aligned}
a''_{00} &= -\frac{\alpha'}{q} - \frac{12}{qWe}\left(\frac{1}{2}a_{01} + a_{02} - a_{20} - a_{21} + a_{40}\right) + \frac{a''_{20}}{2} + \frac{a''_{21}}{8} + \frac{2}{Re}(2a'_{01} + a'_{01})\\
a''_{10} &= -\frac{\beta'}{q} - \frac{2}{qWe}(6a_{10} + 21a_{11} + 18a_{30}) + \frac{3a''_{30}}{2} - \frac{a''_{10}}{2} - \frac{a''_{11}}{4} + \frac{3}{Re}(a'_{30} + 2a'_{11} + 2a'_{30})\\
a''_{20} &= -\frac{\gamma'}{q} - \frac{3}{qWe}\left(21a_{20} - 80a_{40} - 10a_{01} - 40a_{02} + \frac{91}{2}a_{21}\right) + 3a''_{40} - \frac{3a''_{20}}{2} - \frac{3a''_{21}}{4} - \frac{8qa'_{01}}{Re} + \frac{4}{Re}(3a'_{40} + 2a'_{21} + 3a'_{40})\\
a''_{30} &= -\frac{180}{qWe}\left(a_{30} - \frac{1}{2}a_{11}\right) - 3a''_{30} + \frac{1}{4}a''_{11} - \frac{12q}{Re}a'_{11},\\
a''_{40} &= -\frac{\gamma'}{q} - \frac{420}{qWe}\left(a_{40} - \frac{1}{2}a_{21} + \frac{1}{3}a_{02}\right) + \frac{5a''_{21}}{8} - 5a''_{40} - \frac{16q}{Re}a'_{21}\\
a''_{01} &= -\frac{a''_{20}}{2}, \qquad a''_{02} = -\frac{a''_{21}}{8}\\
a'_{11} &= -\frac{3a''_{30}}{2}, \qquad a''_{21} = -3a''_{40}
\end{aligned} \tag{32}$$

where α', β', γ', and δ' are defined as

$$\alpha' = \frac{(3-3n)l}{4(1+lt)^3}, \qquad \beta' = \frac{-nl}{(1+lt)^3}$$
$$\gamma' = \frac{(12n-3)l}{4(1+lt)^3}, \qquad \delta' = \frac{-5nl}{4(1+lt)^3}$$

where $l = 9/8q$ and $n = 9/4$ for an axisymmetric drop. The system of Eq. (32) includes nine linear second-order differential equations for the unknowns $a_{00}, a_{10}, a_{20}, a_{30}, a_{40}, a_{11}, a_{21}, a_{01}, a_{02}$, and their derivatives. These equations can be integrated from time zero, provided that proper initial condition is provided for the mentioned unknowns and their first derivatives at $t = 0$. Because Eq. (31) expresses the velocity of the particles on the interface in the local frame of reference attached to the particle, the initial values of the unknowns $a_{ij}s$ are zero. To calculate the initial value of the $a'_{ij}s$, we can set a_{ij} to zero in Eq. (32) and integrate the equations once with respect to time. Setting $a_{ij} = 0$ in the resulting system of equations, we reach a system of nine algebraic equations for the nine unknown $a'_{ij}s$. Solving the system of algebraic equations, we find the proper initial value for a'_{ij}. For the results that follow, Eq. (32) is integrated using a forth-order Runge–Kutta method using the initial conditions mentioned. The calculated coefficients are plugged back into the series expansion of the local velocities u_z^p and u_r^p. The total velocity of the particles on the interface can be calculated using Eq. (19) and the displacement of the particles on the interface can be calculated by

$$z = \int_0^t u_z(z, r, t)\,\mathrm{d}t, \qquad r = \int_0^t u_r(z, r, t)\,\mathrm{d}t \tag{33}$$

Few comments should be made here regarding the inclusion of some terms, such as the Reynolds number in the system of Eqs. (32). As explained in Gonor and Zolotova [6], inclusion of the viscous terms in their analytical derivations yields an unsolvable system of equations with an infinite number of unknowns. Because the drop deformation in the flow direction z is relatively larger than the cross-stream direction, it is expected that the a_{i0}s in Eq. (32) are the dominant coefficients. A dimensional comparisons between the solution of the a_{ij} in Eq. (32) for various cases approves this argument and shows that the dominant terms in the determination of the deformation of the drop are $a_{i0} (i = 0$ to 4), which represent the first few oscillation modes of the drop. The viscous terms associated to these terms are of a finite number and can be added to the system of

equations as is done in Eq. (32). However, one of the main assumptions on which the theoretical discussions presented in the beginning of the paper are based is that the $Re \sim 1$ and $Oh \sim 1$. Thus, it is not justified to integrate Eq. (32) for small Reynolds numbers. On the other hand, inclusion of the terms involving the Reynolds numbers in the calculations for relatively small Reynolds numbers, increases the computational time to a great extent and distances us from the main goal of this work, which is to provide a fast theoretical–computational scheme for calculating the drop deformation. In summary, the model should be applied to flow conditions that meet the criteria of the assumptions made at the beginning of our discussion, which is mainly a high Reynolds number and a small Ohnesorge number. Fortunately, many practical applications such as those associated with a wide range of spray systems can be studied using the present model.

The next section presents results of calculations for various cases that meet the mentioned criteria. As for one case, which has a relatively small Reynolds number of 40, the viscous terms in Eq. (32) are not included in the integration due to the preceding discussion. This case is included in the results to show how the model can deviate from producing accurate approximations for the drop deformation if the criteria of the model are not well met. Finally, it should be noted that calculations for each case take less than few seconds on an ordinary personal computer. This negligible computational cost is the main merit of this model and enables further implementation of the model in system of multidrops.

3. *Results for an Axisymmetric Drop*

As the first model validation case, Fig. 3 compares the present calculations to experimental results for the case of a water drop at $We = 7.1$, $Re \sim 750$, and $Oh \sim 0.0035$. The ratio a/r_0 is the ratio of the instantaneous radius of the drop in the radial direction a, to the initial radius r_0. This Weber number is below the critical value at which the drop breaks up into smaller drops [4]. Thus, the drop undergoes oscillations of small amplitudes as can be seen in the figure. The effect of viscosity on the deformation of the drop is too small for water drops in the range of $We = 7$–13, and the surface tension is predominant as reported by Hirahara and Kawahashi [4].

As the second case, we consider the deformation of a spherical water drop in airflow with $We \sim 33$, $\mathrm{Re} \sim 4000$, and $Oh \sim 0.001$. At this relatively high Weber number, it is expected that the drop spreads due to the aerodynamic forces exerted on it rather than undergoing small-amplitude oscillations. Figure 4 compares the deformed drop shapes at nondimensional times from 0 to 80 with the experimental data of Gelfand et al [3]. As the figure shows, the windward side of the drop flattens in the early stages. As the deformation grows, the drop begins to spread, and the leeward side takes a flat shape. At this Weber number, the spreading will continue to form a bag shape, which will be followed by bag and shear breakup and mass stripping as reported by Hirahara and Kawahashi [4]. Figure 4b plots the calculated deformation of the drop shown in Fig. 4a and compares it with the experimental values.

As the third comparison case, the deformation of a drop is shown in Fig. 5 for $Re \sim 40$, $We \sim 40$, $Oh \sim 0.15$, and $q \sim 50$. Because the flow conditions do not fall in the desired range of the present model, the calculated model is expected to come short of an accurate prediction of the deformation. To investigate this, we compare the

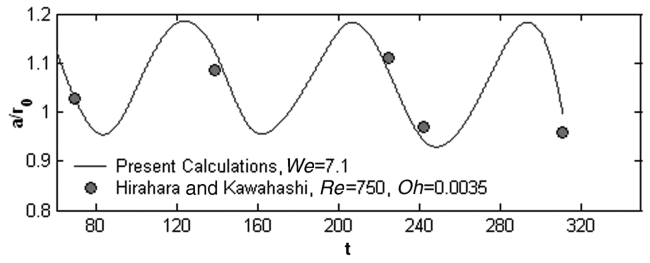

Fig. 3 Comparing calculations to experiments done by Hirahara and Kawahashi [4].

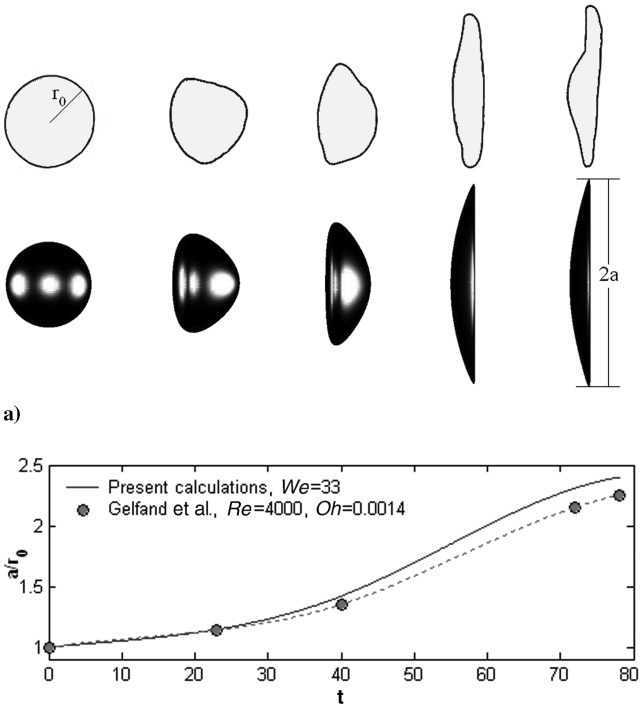

Fig. 4 Image showing a) drop shapes at different times, from left to right $t = 0, 23, 40, 72$, and 78. The top row shows experimental images by Gelfand et al. [3] and the bottom row, present calculations, and b) comparison between the calculated and experimental deformation.

calculated deformation ratio a/r_0 with the results of Quan and Schmidt [10] for a case with exactly the same conditions. Figure 5b shows the comparison.

As discussed at the end of the preceding section, the viscous terms are not included in the calculation of the particular case of Fig. 5

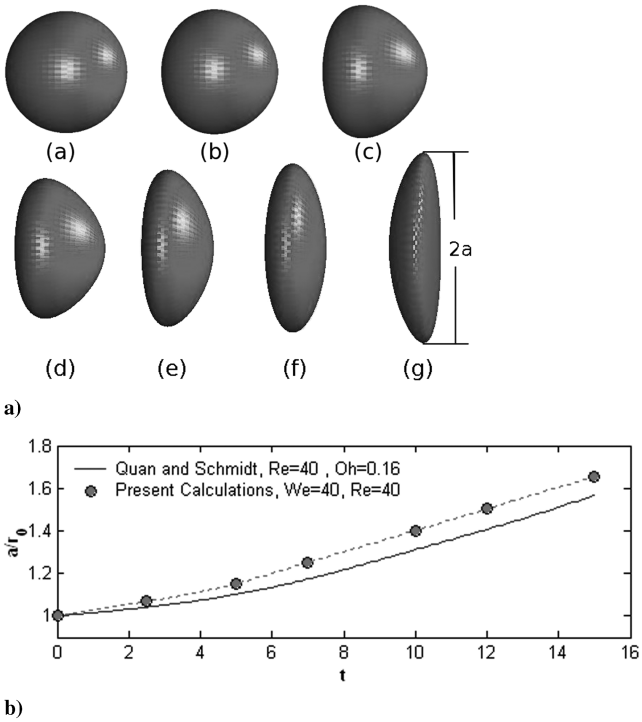

Fig. 5 Image showing a) shape evolution of a spherical drop ($Re = 40$, $We = 40$, and $q = 50$) at nondimensional times $t = 0.0, 2.5, 5.0, 7.0, 10.0, 12.0$, and 15.0, and b) comparison of the deformation with the results of Quan and Schmidt [10].

because the small Reynolds number and the Ohnesorge number do not meet the assumptions of the model. A higher Oh_l, as for this case, indicates that the liquid viscous forces are large compared with the surface tension forces at a constant Weber number. The larger viscous forces within the drop have a stabilizing effect on the drop deformation and breakup as discussed by in Wadhwa et al. [11]. Because the viscous terms are not included for this case, the stabilizing effect due to viscous terms is not affecting the drop deformation. Thus, the drop deformation is over-predicted by the model as clearly seen in Fig. 5b. The overestimation, however, is not extreme at small deformations and will grow larger as the drop spreads more over time [11].

Figure 6 shows the velocity vectors on the drop interface for the same case of Fig. 5. The top row shows the velocities measured in an inertial reference frame. It is observed that the velocity profile on the surface of the drop reaches an almost uniform profile by $t = 15$ (the last drop). The bottom row shows velocities measured in the noninertial frame moving with the drop. From left to right, it is observed that the windward side of the drop is moving toward the center of the drop due to direct contact with the upstream gas flow while the leeward side of the drop is moving backward, with respect to the center of mass of the drop, due to resistance of the gas behind it. As the drop deforms and spreads with time, a pair of double vortices form on the downstream side of it as shown for various cases by Wadhwa et al. [11] and Quan and Schmidt [10]. Close inspection of the bottom row of Fig. 6 shows that the development of the velocity vectors on the downstream side of the drops is consistent with the evolution of the double vortices similar to that shown in Fig. 7 of Quan and Schmidt.

III. Deformation of a Two-Dimensional Drop

Next, we set to modify the formulation developed for an axisymmetric drop to calculate the deformation of a 2-D drop. The main goal of this modification, as will be discussed in detail in the next section, is to provide a tool to describe the deformation of the cross section of a column of liquid injected into a gas stream. Starting from the two-dimensional Navier–Stokes and continuity equations and following a similar procedure to that of Sec. II, we reach

$$
\begin{aligned}
a''_{00} &= -\frac{\alpha'}{q} - \frac{6}{qWe}\left(a_{01} + 2a_{02} - 3a_{20} - \frac{7}{3}a_{21} + 4a_{40}\right) \\
&\quad + a''_{20} + \frac{a''_{21}}{6} + \frac{2}{Re}(a'_{01} + a'_{01}) \\
a''_{10} &= -\frac{\beta'}{q} - \frac{2}{qWe}(6a_{10} + 21a_{11} + 19a_{30}) + 3a''_{30} - a''_{10} \\
&\quad - \frac{a''_{11}}{3} - \frac{4q}{Re}a'_{10} + \frac{2}{Re}(3a'_{30} + 2a'_{11} + 3a'_{30}) \\
a''_{20} &= -\frac{\gamma'}{q} - \frac{12}{qWe}\left(6a_{20} - 33a_{40} - 2a_{01} - 9a_{02} + \frac{39}{3}a_{21}\right) \\
&\quad + 6a''_{40} - 3a''_{20} - a''_{21} - \frac{4q}{Re}(3a'_{20} + 2a'_{01}) \\
&\quad + \frac{6}{Re}(4a'_{40} + a'_{21} + 2a'_{40}) \\
a''_{30} &= -\frac{240}{qWe}\left(a_{30} - \frac{a_{11}}{3}\right) - 6a''_{30} + \frac{a''_{11}}{3} - \frac{12q}{Re}(2a'_{3} + a'_{11}) \\
a''_{40} &= -\frac{\gamma'}{q} - \frac{600}{qWe}\left(a_{40} - \frac{a_{21}}{3} + \frac{a_{02}}{5}\right) + \frac{5a''_{21}}{6} \\
&\quad - 10a''_{40} - \frac{2q}{Re}(10a'_{40} - 4a'_{21}) \\
a''_{01} &= -a''_{20}, \qquad a''_{02} = -\frac{a''_{21}}{6} \\
a'_{11} &= -3a''_{30}, \qquad a''_{21} = -6a''_{40}
\end{aligned}
\tag{34}
$$

where α', β', γ', and δ' are defined as in the previous section. However, $l = 2/q$ and $n = 4$ in the case of the 2-D drop. The numerical scheme used to solve for the system of equations noted in Eq. (34) is the same as the axisymmetric case. The initial conditions are calculated the same way, and the equations are integrated to solve for the velocity expansion coefficients a_{ij}, and to calculate the perturbation velocities

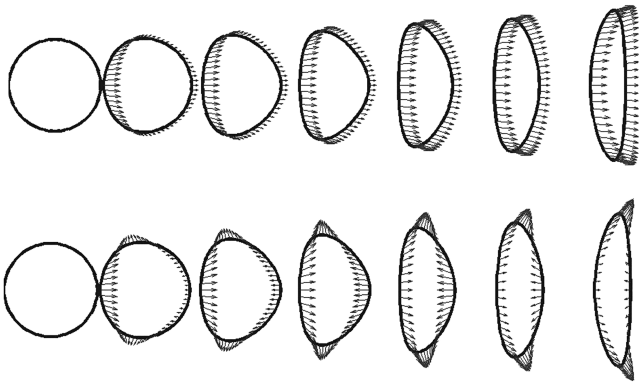

Fig. 6 The interface velocity for the same case as in Fig. 4. The top row shows velocities measured in an inertial frame, and the bottom row shows velocities measured in the noninertial frame.

$$
x = \int_0^t u_x(x, y, t)\,\mathrm{d}t, \qquad y = \int_0^t u_y(x, y, t)\,\mathrm{d}t \tag{35}
$$

where x and y are the local coordinates of the particles on the drop interface in the gas-stream and the cross-stream directions, respectively. It should be noted that several modifications are necessary from the axisymmetric case to the 2-D drop calculations, among which are using the potential flow over a circle or ellipse when necessary, using a proper smoothing function, providing the proper pressure distribution on the sphere [similar to the discussion presented after Eq. (30)], and considering the changes in geometrical parameters such as the mean curvature.

To illustrate the substantial difference between the spreading of axisymmetric and 2-D drops, Fig. 7 compares the deformation of a 2-D drop to an axisymmetric drop at equal flow conditions. For the case of the axisymmetric drop, the gas flow can travel around the drop, although this is not feasible in the 2-D case. Thus, the gas can only travel in the transverse direction in the 2-D case, which rapidly spreads the drop in the cross-streamwise direction. As shown in the last frames, the large shear force exerted at the tips of the deformed drop by the gas stream elongates the drop in the direction of the gas

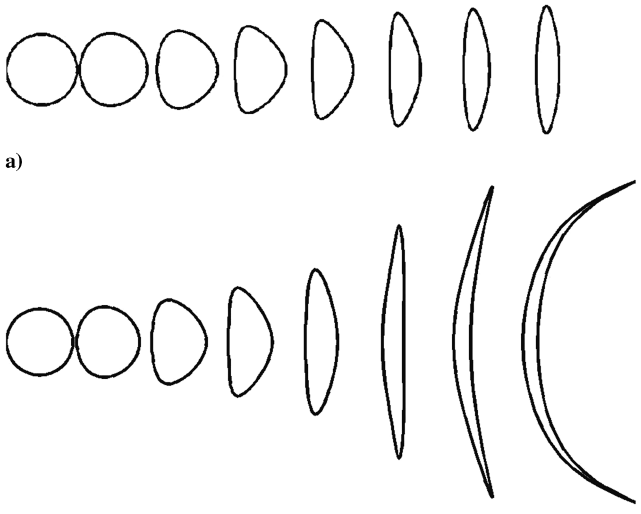

a)

b)

Fig. 7 Comparison between the deformation of an axisymmetric water drop (top row) with that of a 2-D water drop (bottom row) in air with $We = 35$. The times from left to right are $t = 0, 10, 20, 30, 40, 50, 55$, and 58.

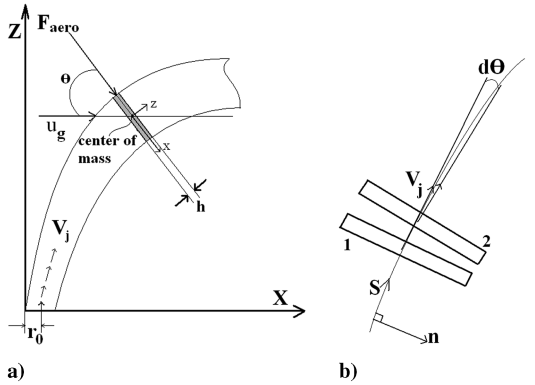

Fig. 8 Image showing a) the schematic of a liquid jet travelling in a crossflow, and b) the motion of the cross-sectional element during time d*t*.

flow. It is known that the shear forces around a 2-D drop are higher and the surface tension forces are lower than that of spherical drops. In 2-D cases, the curvature is only present in one plane although for spherical drops the curvature is present at two perpendicular planes and allows for the drop to deform spatially rather than a two-dimensional rapid deformation.

IV. Deformation of a Liquid Jet in a Crossflow

In this section, we apply the scheme developed in the previous section to model the deformation of a liquid jet injected normal to a subsonic gaseous flow. Both the gas flow and the liquid jet flows are assumed to be nonturbulent. Figure 8a demonstrates a schematic of a jet deforming and traveling in the crossflow. As the figure shows, the jet deflects due to the aerodynamic force acting on it.

As the injected jet travels transversely into the gas stream, drops and fragments strip from the liquid column. The starting point and the rate of mass shedding depend on the gas flow conditions and the breakup regime. Several authors have studied the breakup regimes associated with this type of injection [16,17]. In general, the breakup regime is classified with respect to the gas Weber number. At low Weber numbers, the breakup type is bag breakup, and it changes to bag-shear and shear-dominant breakup as the gas Weber number increases. Mazallon et al. [12] also studied the breakup regimes of liquid jets injected into a crossflow over a wide range of test conditions and liquid properties. Their study suggested that mass

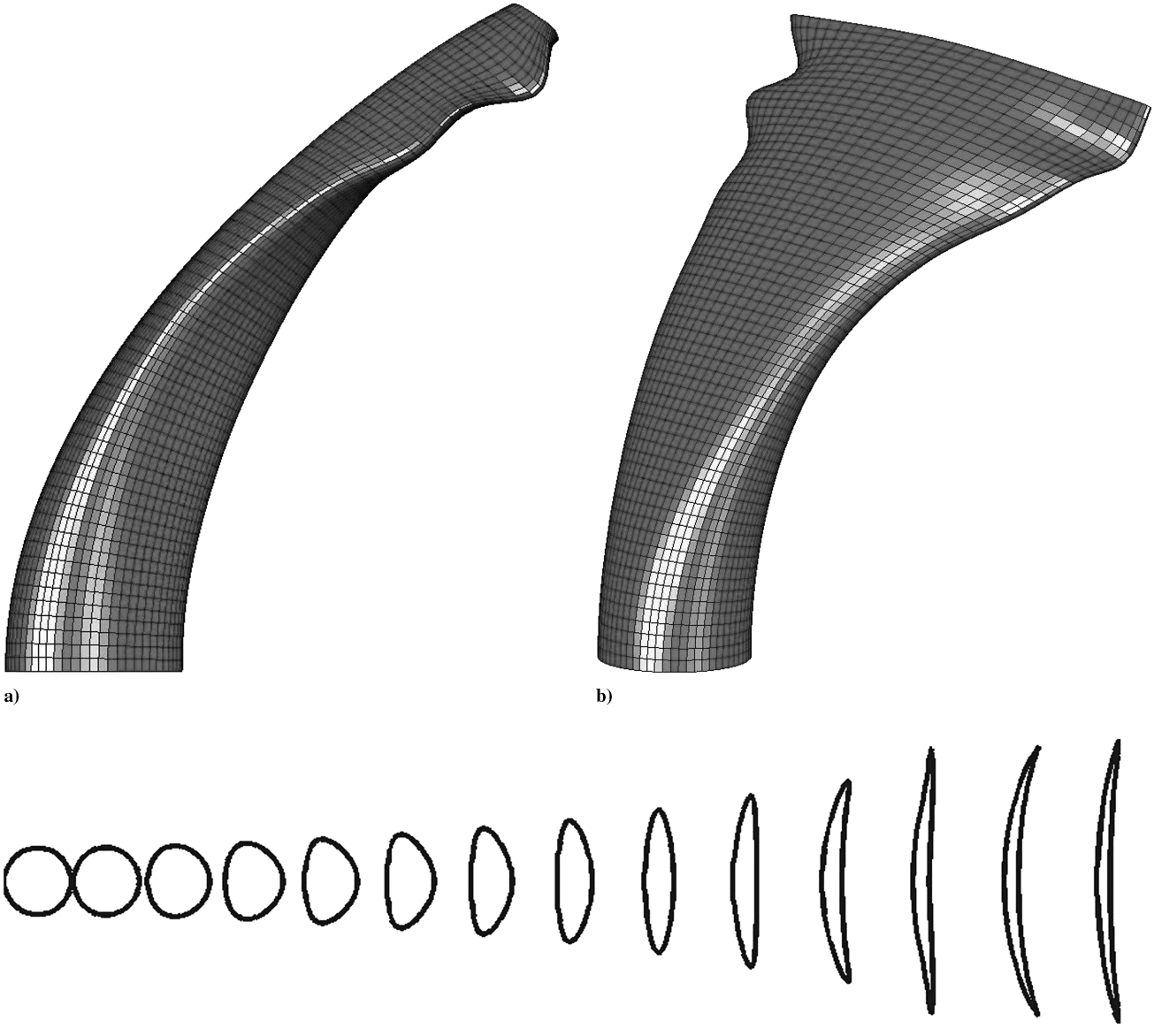

Fig. 9 Deformation of a water liquid jet in air stream at *We* = 35 with a) side view, b) 35 deg view, and c) the evolution of the jet's cross section from the nozzle to the tip.

stripping from the jet does not occur unless the Weber number is larger than a critical value (∼60 for nonturbulent cases). In this section, we consider cases with Weber numbers below this critical value so that mass stripping would not have an effect on the results. This way, we can focus on the deformation of the liquid jet by focusing on the oscillations of its cross section. Mashayek et al. [14] studied the deformation and deflection of a liquid jet in crossflow using a two-dimensional elliptic model, which allowed for deformation of the jet cross section from an initial circle to elongated ellipses. They assumed that the jet velocity is constant along its trajectory up to the breakup location and calculated the trajectory using a force balance. To calculate the displacement of the drop, they balanced the forces in the cross-sectional plane using a numeric-based local drag coefficient and the frontal area of the cross-sectional element with unit thickness. We shall use their work as a starting point here to predict the trajectory of liquid jets in crossflow in subcritical (no stripping) flows. Similarly, we assume a cross-sectional liquid element with unit thickness as shown in Fig. 8a. Next, we decompose the motion of the liquid jet into the motion of the cross-sectional element with respect to a local coordinate system attached to the element (shown by small letters in the figure) and the motion of the noninertial local coordinate system with respect to the inertial frame (shown by capital letters in the figure). Thus, the equation of motion governing the motion of the two-dimensional cross section of the liquid jet written in the local noninertial frame attached to the center of mass of the cross-sectional element is

$$\frac{\partial \mathbf{u}}{\partial t} + \mathbf{u} \cdot \nabla \mathbf{u} = -\frac{1}{k}\nabla p + \frac{1}{Re}(\nabla^2 \mathbf{u}) + \mathrm{F}^{\mathrm{Inertial}} \tag{36}$$

where $\mathbf{F}^{\mathrm{Inertial}}$ is the fictitious inertial force defined by

$$\mathbf{F}^{\mathrm{Inertial}} = -\frac{\mathrm{d}\mathbf{U}_l}{\mathrm{d}t} - 2\Omega \times \mathbf{u} - \Omega \times (\Omega \times \mathbf{x}) - \frac{\mathrm{d}\Omega}{\mathrm{d}t} \times \mathbf{x} \tag{37}$$

where $\mathbf{U}_l$ is the velocity of the noninertial coordinate system with respect to the global system, $\mathbf{\Omega}$ is the angular velocity vector of the noninertial coordinate system, and $\mathbf{u}$ and $\mathbf{x}$ are the velocity and position vectors of the liquid particles with respect to the local noninertial coordinate system. To ensure that the conservation of mass is satisfied in the absence of the mass stripping, we also assume that the velocity of the jet is constant in the direction normal to its cross section. This assumption along with the Eqs. (36) and (37) and the method developed in the preceding section can be used to predict the penetration of the liquid jet. The deformation of the cross section of the liquid column can be calculated using the two-dimensional model explained in detail in the preceding section with two modifications. The first modification is the addition of the inertial forces according to Eq. (37). Second, it should be noted that the velocity of the incident gas flow and the velocity of the cross-sectional element with respect to its local coordinate are not in the same direction anymore as shown in Fig. 8a. Thus, as done by Mashayek et al. [14], the relative velocity between the gas and the liquid should be modified by projecting the gas flow onto the cross-sectional plane as shown by $\mathbf{F}_{\mathrm{aero}}$ in the figure. The angle θ is the instantaneous angle the element's plane makes with the gas direction. To calculate this angle, we focus on Fig. 8b, which shows the motion of the element in an infinitesimal period of time, dt. During this time, the element rotates by angle dθ. As the figure shows, the center of mass of the element at time $t + \mathrm{d}t$ (element marked 2) has moved by an amount of dx and dy, with respect to the local coordinate system attached to the element at time t (element marked 1). Noting that the jet velocity is assumed constant in the direction normal to the cross section 1, the partial displacements of the element 2 with respect to 1 are $\mathrm{d}x = u_{\mathrm{cm}}$ and $\mathrm{d}y = v_j$ where u_{cm} is the velocity of the center of mass of the two-dimensional section calculated using the 2-D model and v_j is the nondimensional injection velocity of the jet. Thus, dθ can be calculated using

$$\mathrm{d}\theta = \mathrm{d}y/\mathrm{d}x = v_j/u_{\mathrm{cm}} \tag{38}$$

at each instant. Equation (38) can be integrated over time to calculate θ at each time and can also be used to calculate the angular velocity and acceleration of the noninertial coordinate system required for calculating the terms in Eq. (38).

To demonstrate the procedure explained previously, Fig. 9 shows the cross-sectional deformation of a liquid jet along with the constructed liquid jet. As we know, an axisymmetric or a two-dimensional drop undergoes small-amplitude oscillations at low Weber numbers. However, for large Weber numbers, the deformation in the drop is not reversible, and the drop undergoes an irreversible spreading [4]. Because the Weber number of the case shown in Fig. 9 is 35, there is no bounce back in the motion of the liquid column's cross section. To understand the reason behind the curly shape observed on the edge of the flattened jet, Figs. 9a–9c show the deformation of jet cross section over time. The back and forth movement of the tip of the cross section leads to the wave-like shape formed on the jet surface.

Figure 10 compares the deformation and penetration of two liquid jets with momentum ratios of $M = 9.54$ and $M = 1.94$ with results of Madabhushi et al. [18]. The momentum ratio, defined as $M = \rho_l u_l^2/\rho_g u_g^2$, is an important parameter in studying the JICF problem and has been widely used as the key parameter in characterizing the penetration of the liquid jet in various conditions. Because the Weber numbers of the cases in Fig. 10 are relatively small, no mass is shed from the liquid column, and the jet cross section shows oscillatory motion as shown in the side view figures. As the calculated jets (right panels) in both cases show, the bounce back of the cross section of the jet seems to be exaggerated compared with the experiments in the left panels. This difference is more pronounced in case (b) where the liquid jet has a smaller velocity and, thus, more oscillations of the jet cross section can be observed within the limits of the image. The main reason behind this difference might be the fact that the viscous effects are not fully incorporated in the modeling especially in the third dimension (direction normal to the cross section along the trajectory of the center of mass of an element). This leads to an almost complete bounce back of the cross section to its initial circular shape unlike the flatter experimental jets. The less flat (or more circular) the shape of the calculated jet, the smaller the

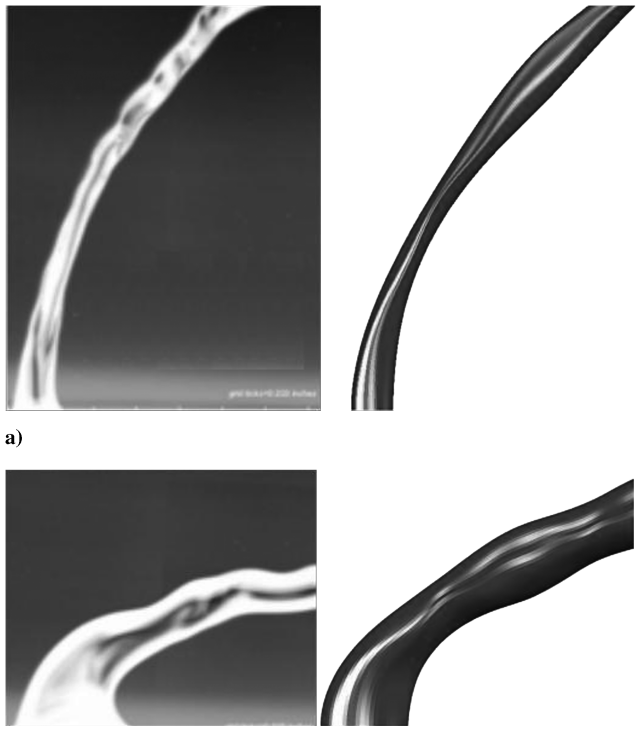

a)

b)

Fig. 10 Comparison between present calculations (right) and the experimental results reproduced from Madhabushi et al. [18] by permission (left) where a) $q = 9.54$, $Re_l = 1007$, and b) $q = 1.94$, $Re_l = 454$.

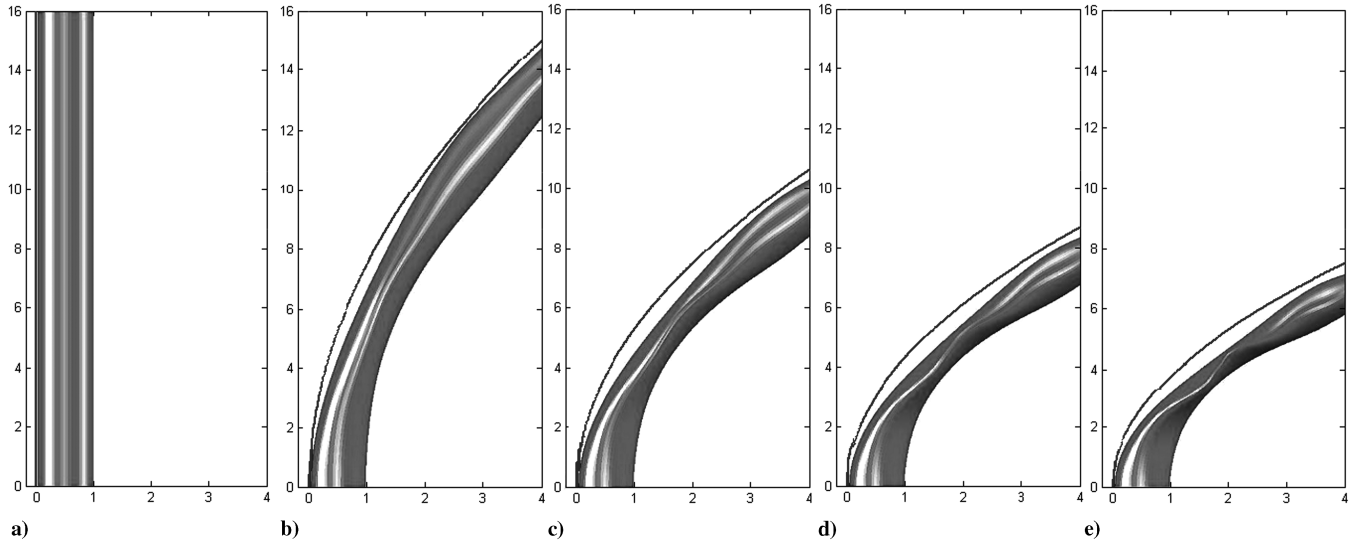

Fig. 11 Side view of the deformation and penetration of water jets in an air stream. a) $We = 0, q = \infty$, b) $We = 5, q = 30$, c) $We = 10, q = 15$, d) $We = 15, q = 10$, e) $We = 20, q = 7.5$. The solid lines show the trajectory curves obtained using the correlation of Wu et al. [16].

aerodynamic drag force acting on the jet column becomes. This causes the calculated jet to penetrate more into the gas stream as clearly seen in case (b). Although one cannot expect to capture all three-dimensional characteristics of the deformation of the liquid jet using the two-dimensional mapping system of the present model, the resemblance of the calculated jet shapes to the experimental figures supports the similarities between the deformation and oscillation characteristics of liquid drops and jets in crossflow reported previously by various authors. However, it is important to note that the current model is incapable of resolving the complicated physical aspects of the jet deformation and is only a means to provide a better estimation of the jet trajectory compared with some primitive theoretical models available to date.

To further verify the model, we investigate the effect of changing the momentum ratio and Weber number on the deformation and penetration of the jet. Figure 11 shows the side view of five water jets in airflow with common jet velocities of 4.7 (m/s) and various air velocities. The Weber number changes from 0 in the first frame to 15 in the last frame while the momentum ratio changes from ∞ in the first frame to 7.5 in the last frame. It is clear that as the momentum ratio decreases from left to right, the jet penetrates less into the cross stream as reported by all the previous studies on the JICF problem. The figure also shows that with an increase in the Weber number from left to right, the cross-sectional deformation grows larger. Solid lines drawn on the calculated jets in Fig. 11 show the jet trajectories predicted using the empirical correlation of Wu et al. [16]. As the figure shows, the present model predicts the jet penetration well for jets without mass stripping. The calculation time of each penetration curve is very short while the physical parameters of the interior and exterior of the problem are accounted for. This makes this model superior to correlations and formulae, which contain the momentum ratio as the mere parameter in determination of the penetration of the liquid jet. One can also take the effect of mass stripping partially into account by considering the amount of mass shed from the jet over time and impose the mass reduction in the form of a reduction in the cross-sectional area of the jet. This is similar to the procedure followed in Mashayek et al.[14] and is fairly straight forward to apply.

V. Conclusion

The deformation of inviscid axisymmetric drops was studied employing an existing model with some modifications and a new numerical solutions scheme. The model was validated by comparisons made with experiments. The model was also modified for two-dimensional drops. The results showed considerable difference between the behaviors of a two-dimensional and an axisymmetric drop in the same flow conditions. The spreading of a two-dimensional drop was used as a base model to simulate the deformation of the cross section of a liquid jet in a gaseous crossflow at relatively low Weber numbers. The results were in agreement with the experimental reports. The calculations support the similarities between the deformation of a liquid column and spreading of a drop in the crossflow as reported in the literature. The combination of the tools provided in this work can help in modeling the penetration of a liquid jet in a crossflow and, with the addition of mass stripping to the model, can be used to model the deformation and spreading of the drops produced from primary and secondary breakup mechanisms associated with the jet disintegration. The significance of the present model is its extreme speed (in the order of few seconds for each case on a regular PC), which makes it an appropriate option for parametric studies. The low cost of the numerical scheme places this model among fast yet accurate models that can be used to model drop deformation in spray systems.

References

[1] Wierzba, A., "Deformation and Breakup of Liquid Drops in a Gas Stream at Nearly Critical Weber Numbers," *Experiments in Fluids*, Vol. 9, No. 1, 1990, pp. 59–64. doi:10.1007/BF00575336

[2] Ranger, A. A., and Nicholls, J. A., "Aerodynamic Shattering of Liquid Drops," *AIAA Journal*, Vol. 7, No. 2, 1969, pp. 285–290. doi:10.2514/3.5087

[3] Gelfand, B. E., Gubin, S. A., and Kogarko, S. M., "The Varieties of Drop Breakup Behind the Shock Waves and Their Characteristics," *Journal of Engineering Physics and Thermophysics*, Vol. 27, No. 1, 1974, pp. 119–126 (in Russian).

[4] Hirahara, H., and Kawahashi, M., "Experimental Investigation of Viscous Effects upon a Breakup of Drops in High-Speed Air Flow," *Experiments in Fluids*, Vol. 13, No. 6, 1992, pp. 423–428. doi:10.1007/BF00223250

[5] Harper, J. F., and Moore, D. W., "The Motion of a Spherical Liquid Drop at High Reynolds Number," *Journal of Fluid Mechanics*, Vol. 32, No. 2, 1968, pp. 367–391. doi:10.1017/S0022112068000789

[6] Gonor, A. L., and Zolotova, N. V., "Spreading and Break-Up of a Drop in a Gas Stream," *Acta Astronautica*, Vol. 11, No. 2, 1984, pp. 137–142. doi:10.1016/0094-5765(84)90004-3

[7] Fornberg, B., "Steady Viscous Flow Past a Sphere at High Reynolds Numbers," *Journal of Fluid Mechanics*, Vol. 190, 1988, pp. 471–489. doi:10.1017/S0022112088001417

[8] Helenbrook, B. T., and Edwards, C. F., "Quasi-Steady Deformation and Drag of Uncontaminated Liquid Drops," *International Journal of Multiphase Flow*, Vol. 28, No. 10, 2002, pp. 1631–1657. doi:10.1016/S0301-9322(02)00073-3

[9] Constantinescu, G., and Squires, K., "Numerical Investigation of Flow

Over a Sphere in the Subcritical and Supercritical Regimes," *Physics of Fluids*, Vol. 16, No. 5, 2004, p. 1449.
doi:10.1063/1.1688325

[10] Quan, S., and Schmidt, D. P., "Direct Numerical Study of a Liquid Drop Impulsively Accelerated by Gaseous Flow," *Physics of Fluids*, Vol. 18, No. 10, 2006, p. 102103.
doi:10.1063/1.2363216

[11] Wadhwa, A. R., Magi, V., and Abraham, J., "Transient Deformation and Drag of Decelerating Drops in Axisymmetric Flows," *Physics of Fluids*, Vol. 19, No. 11, 2007, p. 113301.
doi:10.1063/1.2800038

[12] Mazallon, J., Dai, Z., and Faeth, G. M., "Primary Breakup of Nonturbulent Round Liquid Jets in Gas Crossflows," *Atomization and Sprays*, Vol. 9, No. 3, 1999, pp. 291–311.

[13] Nguyen, T. T., and Karagozian, A. R., "Liquid Fuel Jet in Subsonic Crossflow," *Journal of Propulsion and Power*, Vol. 8, No. 1, 1992, pp. 21–29.
doi:10.2514/3.23437

[14] Mashayek, A., Jafari, A., and Ashgriz, N., "Improved Model for the Penetration of Liquid Jets in Subsonic Crossflows," *AIAA Journal*, Vol. 46, No. 11, 2008, pp. 2674–2686.
doi:10.2514/1.28254

[15] Pozrikidis, C., *Introduction to Theoretical and Computational Fluid Dynamics*, Oxford Univ. Press, New York, 1997.

[16] Wu, P. K., Kirkendall, K. A., Fuller, R. P., and Nejad, A. S., "Breakup Processes of Liquid Jets in Subsonic Crossflow," *Journal of Propulsion and Power*, Vol. 13, No. 1, 1997, pp. 64–73.
doi:10.2514/2.5151

[17] Becker, J., and Hassa, C., "Breakup and Atomization of a Kerosene Jet in Crossflow at Elevated Pressure," *Atomization and Sprays*, Vol. 12, Nos. 1–3, 2002, pp. 49–67.
doi:10.1615/AtomizSpr.v12.i123.30

[18] Madabhushi, R. K., Leong, M. Y., Arienti, M., Brown, C. T., and McDonell, V. G., "On the Break-Up Regime Map of Liquid Jet in Crossflow," *19th Annual Conference on Liquid Atomization and Spray Systems*, Institute for Liquid Atomization and Spray Systems, Toronto, May 2006.

P. Givi
Associate Editor